Energetic Rupture and Tsunamigenesis during the 2020 $M_{\rm w}$ 7.4 La Crucecita, Mexico Earthquake

Diego Melgar^{*1}, Angel Ruiz-Angulo², Xyoli Pérez-Campos³, Brendan W. Crowell⁴, Xiaohua Xu⁵, Enrique Cabral-Cano³, Michael R. Brudzinski⁶, and Luis Rodriguez-Abreu⁷

Abstract

The La Crucecita earthquake ruptured on the megathrust, generating strong shaking and a modest but long-lived tsunami. This is a significant earthquake that illuminates important aspects of the behavior of the megathrust as well as the potential related hazards. The rupture is contained within 15–30 km depth, ground motions are elevated, and the energy to moment ratio is high. We argue that it represents a deep megathrust earthquake, the 30 km depth is the down-dip edge of slip. The inversion is well constrained, ruling out any shallow slip. It is the narrow seismogenic width and the configuration of the coastline that allow for deformation to occur offshore. The minor tsunamigenesis can be accounted for by the deep slip patch. There is a significant uplift at the coast above it, which leads to negative maximum tsunami amplitudes. Finally, tide-gauge recordings show that edge-wave modes were excited and produce larger amplitudes and durations in the Gulf of Tehuantepec.

Cite this article as Melgar, D., A. Ruiz-Angulo, X. Pérez-Campos, B. W. Crowell, X. Xu, E. Cabral-Cano, M. R. Brudzinski, and L. Rodriguez-Abreu (2020). Energetic Rupture and Tsunamigenesis during the 2020 $M_{\rm w}$ 7.4 La Crucecita, Mexico Earthquake, *Seismol. Res. Lett.* **XX**, 1–11, doi: 10.1785/0220200272.

Supplemental Material

Introduction

The 23 June 2020 $M_{\rm w}$ 7.4 La Crucecita, Mexico earthquake (Fig. 1) nucleated in the southeast of the state of Oaxaca at 15:29:03.0 UTC at a depth of 21 km. The location and the low-angle thrust faulting mechanism are consistent with the expected location of the megathrust in the region (Pardo and Suárez, 1995; Melgar and Pérez-Campos, 2011; Hayes et al., 2018). Convergence rates in the Mexican subduction zone (MSZ) increase systematically from north to south and in this part of the country are about 70 mm/yr (DeMets et al., 2010); similarly, interseismic coupling has been inferred to be high (at least 50%) throughout the state between -99.0° and -95.5° longitude (Rousset et al., 2017). Farther east of the Tehuantepec ridge (Fig. 1) coupling is interpreted to remain high, at least, to the Mexico-Guatemala border (Franco et al., 2012), although, given the long continental shelf, the resolution of the locking models offshore can be quite limited.

As a result of the active tectonics in the region, large earth-quakes are common. Figure 1 shows aftershock areas of large events going back to 1965 and the slip regions of three modern events—the 1995 $M_{\rm w}$ 7.3 Copala, 2012 $M_{\rm w}$ 7.5 Ometepec, and 2018 $M_{\rm w}$ 7.2 Pinotepa earthquakes (Courboulex *et al.*, 1997; UNAM Seismology Group, 2013; Li *et al.*, 2020). Singh *et al.* (1981,1983) noted that large events in this part of the MSZ have a characteristic magnitude of $\sim M_{\rm w}$ 7.5 and an average recurrence of 30–50 yr. Interestingly, the 2012 Ometepec earthquake occupies the same location as the aftershock area

of the 1982 doublet (Astiz and Kanamori, 1984), the Pinotepa earthquake reoccupies a significant portion of the aftershock area of the 1968 $M_{\rm w}$ 7.3 earthquake (Chael and Stewart, 1982), whereas the La Crucecita earthquake nucleates within the aftershock region of the 1965 $M_{\rm w}$ 7.5 earthquake (Chael and Stewart, 1982).

Two important patterns are suggested from previous events. During large earthquakes, rupture rarely, if ever, extends below the 30 km depth contour of the subducted slab. The only exception to this is the 1965 aftershock area, which is poorly constrained by the data (UNAM Seismology Group, 2013). This indicates that, perhaps, this is the down-dip edge of coseismic slip; an important demarcation to identify, because it is a key constraint for evaluating the seismic hazard of the region. At deeper depths transient deformation from slow slip events (SSEs) and much weaker seismic release in the form of tectonic tremor have been well documented (Kostoglodov *et al.*,

^{1.} Department of Earth Sciences, University of Oregon, Eugene, Oregon, U.S.A.;

^{2.} Icelandic Meteorological Office, Veðurstofa Íslands, Reykjavík, Iceland.; 3. Instituto de Geofísica, Universidad Nacional Autónoma de México, Circuito de la Investigación Científica S/N, Ciudad Universitaria, Coyoacán, México CDMX, México;

^{4.} Department of Earth and Space Sciences, University of Washington, Seattle, Washington, U.S.A.; 5. Scripps Institution of Oceanography, University of California San Diego, San Diego, California, U.S.A.; 6. Department of Geology & Environmental Earth Science, Miami University, Oxford, Ohio, U.S.A.; 7. Grillo Sistemas, México City, Tlaxcala No. 36, México

^{*}Corresponding author: dmelgarm@uoregon.edu

[©] Seismological Society of America

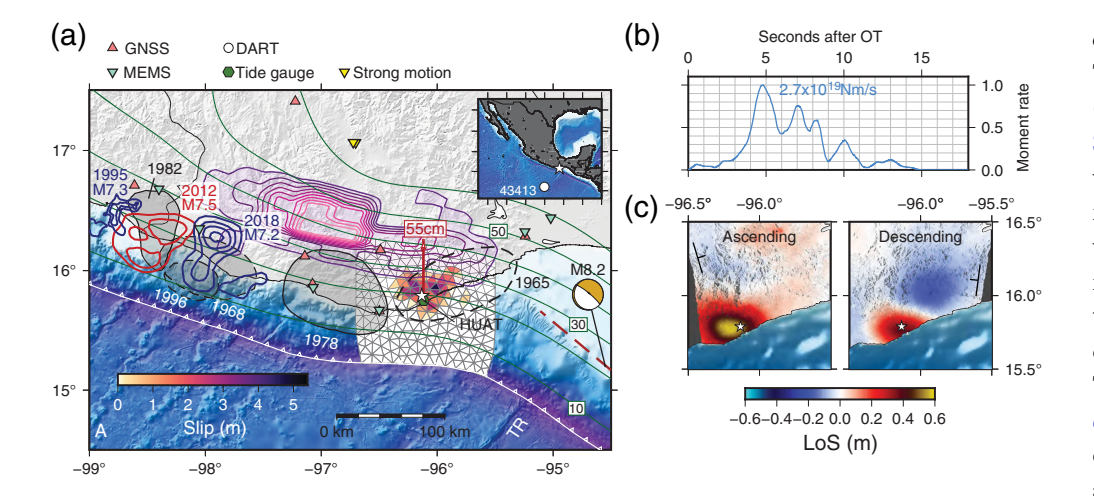


Figure 1. (a) Tectonic context and slip inversion results. The surface used for inversion is shown as triangles colored by the amount of slip. White star is the epicenter. The different station types are shown as well. Green contours are the depths to the slab from Slab 2.0 (Hayes *et al.*, 2018) at 10 km intervals. Blue and red contours are slip models for past large events in the region (Courboulex *et al.*, 1997; UNAM Seismology Group, 2013; Li *et al.*, 2020). Shaded gray regions are aftershock areas of older events of the 20th century. Those indicated with dashed lines are less well constrained (UNAM Seismology Group, 2013). Purple shaded contours at 10 mm intervals are the slow slip event preceding the 2012 Ometepec earthquake (Graham *et al.*, 2014a). Red arrow indicates 55 cm of coseismic uplift measured at the Huatulco (HUAT) tide gauge. The moment tensor is for the 2017 $M_{\rm w}$ 8.2 Tehuantepec earthquake. Brown dashed line is the surface projection of its causative fault (Melgar *et al.*, 2018a). TR is the Tehuantepec Ridge. (b) Event source time function. (c) Line of sight (LoS) deformation from ascending and descending tracks, positive is motion toward the satellite. White star is the same epicenter as in (a). The color version of this figure is available only in the electronic edition.

2003; Brudzinski *et al.*, 2010; Graham *et al.*, 2015). In Oaxaca, this occurs largely at depths deeper than 40 km; however, shallow slow-slip has also been identified and hypothesized to have contributed to triggering the 2012 Ometepec-Pinotepa Nacional earthquake (Graham *et al.*, 2014a; Colella *et al.*, 2017).

The second pattern that emerges is the dearth of slip at depths shallower than ~10 km. This is consistent with the observation that the tsunami record in Mexico shows a predominance of modestly sized events with coastal amplitudes in the \sim 1-2 m range (e.g., Ramírez-Herrera et al., 2012; Corona and Ramirez-Herrera, 2012). Only two large tsunamigenic events have been identified, the 1932 M_s 8.2 event in Jalisco at the northern edge of the subduction zone (Corona and Ramirez-Herrera, 2012) and the 1787 ~M 8.6 San Sixto earthquake offshore Oaxaca (Suárez and Albini, 2009) whose tsunami deposits have been identified several kilometers inland (Ramírez-Herrera et al., 2020). Despite most tsunamis being of modest amplitude, for the Gulf of Tehuantepec (east of -96° longitude), there is an added hazard. The wide, shallow, and flat shelf very efficiently traps tsunami energy in the form of edge waves and through wholesale resonance of the shelf (Melgar and Ruiz-Angulo, 2018). As a result, comparatively small events can be amplified and can last for many hours. This was the case during the 2017 $M_{\rm w}$ 8.2 Tehuantepec earthquake (Fig. 1, Melgar et al., 2018a; Suárez et al., 2019). That event was a relatively deep (~50 km), normal-faulting earthquake, with limited coseismic deformation, which nonetheless led to an ~3 m tsunami at the of Gulf coasts the of Tehuantepec (Ramírez-Herrera et al., 2018). The tsunami was observed at coastal tide gauges above the background noise for almost 48 hr (Melgar and Ruiz-Angulo, 2018).

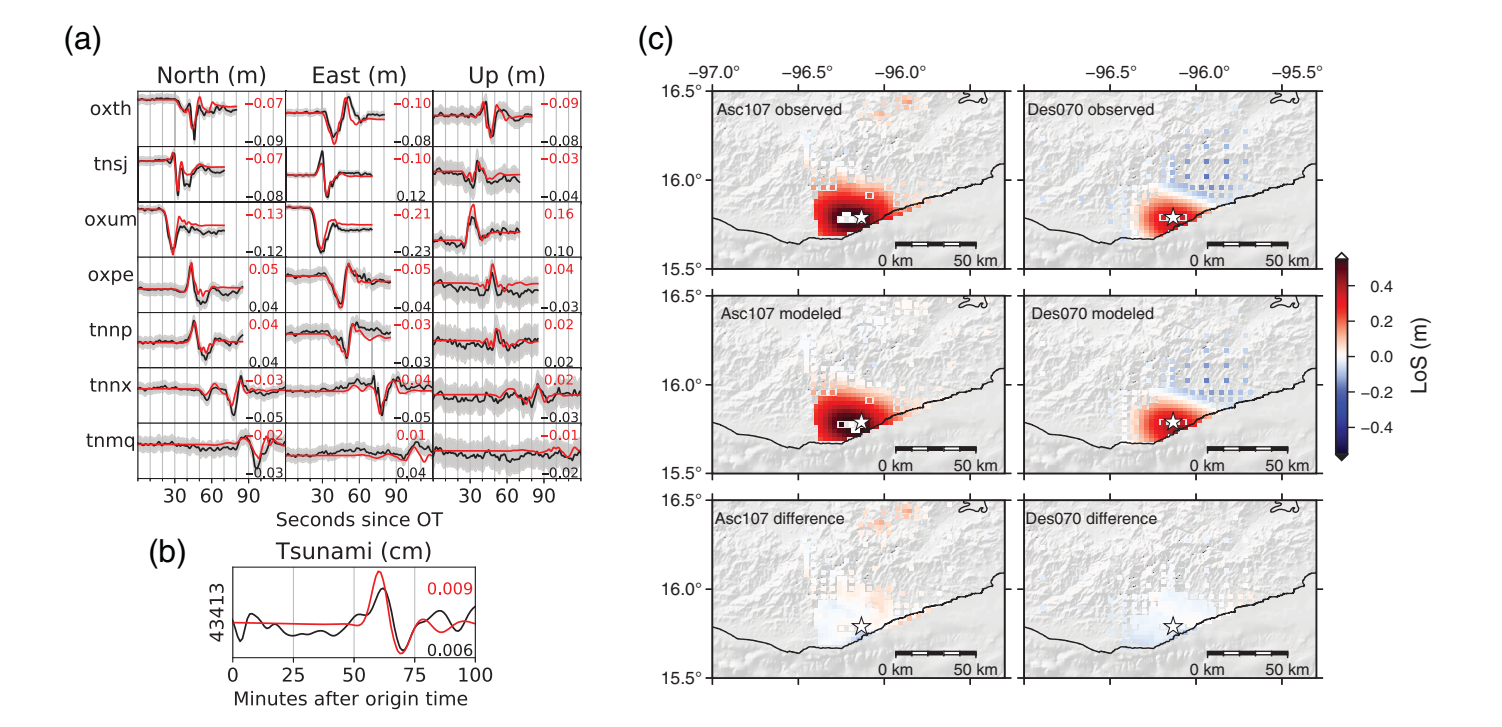
Within this context, the 2020 earthquake is important. It occurs within the aftershock region of a previously identified large earthquake. It was observed by varied regional geophysical instrumentation (Fig. 1), including high-rate Global Navigation Satellite (HR-GNSS) System data, strong motion, tide gauge, ocean-bottom pressure, novel micro-electromechanical

(MEMS) accelerometers, and by Interferometric Synthetic Aperture Radar (InSAR). Here, we will show that the rupture was relatively simple with one well-defined asperity but with an energetic source process that led to slightly elevated ground motions and which is consistent with rupture close to the down-dip edge of slip. We conclusively establish that there is no shallow slip and show that a large portion of the coast is significantly uplifted, leading to negative peak tsunami values (drawdown of the ocean), helping to explain why tsunamis are not always well recorded in the geologic record in Mexico. Finally, we will discuss how, within the Gulf of Tehuantepec, this event excited edge waves, which led to larger amplitudes within the shelf and to a longer duration of the event like in 2017. Though the tsunami in the 2020 La Crucecita earthquake was not particularly damaging, it serves as a reminder of the continued existence of tsunami hazards in the region.

Methods and Data

Observations and processing

Geodetic data. We computed 5 Hz displacement and velocity waveforms for seven stations from the TLALOCNet GNSS network (Cabral-Cano *et al.*, 2018). The full displacement waveforms, not just the static offsets, are used for slip inversion. These were obtained using the relative positioning



algorithm implemented in the TRACK software (Herring et al., 2010). We use station UXAL 450 km north of the event as a reference. Only the first 100 s of information after the earth-quake origin-time are analyzed, and no motion at the reference site is propagated into the solutions (Fig. 2). The velocity waveforms (Fig. S1, available in the supplemental material to this article), which are used to study the ground-motion intensities, are obtained using the variometric technique described by Colosimo et al. (2011).

For inversion we also use InSAR line-of-sight measurements from two tracks from the Sentinel-1A/1B satellites operated by the European Space Agency (Fig. 1, and Figs. S2 and S3). For ascending track 107 and descending track 070 (Fig. 1), the interferometric pairs span the dates 19-25 June 2020 and 22-28 June 2020, respectively. The Sentinel-1 data are coregistered purely using geometric information (Xu et al., 2017); and, the interferometric phase is calculated using the GMTSAR software (Sandwell et al., 2016), with postprocessing done with Generic Mapping Tools (Wessel et al., 2019). A 200 m low-pass filter is applied to suppress phase noise, and interferograms from different sub-swaths are stitched together and then unwrapped using the statistical-cost network-flow algorithm for phase unwrapping (SNAPHU) (Chen and Zebker, 2002). Before phase maps are unwrapped, all pixels in the ocean are interpolated to their nearest neighbor to allow proper phase change along the coastline. Linear ramps are removed using data far away from the area of coseismic deformation to correct long-wavelength atmospheric noise and potential orbital errors. The line of sight data is then subsampled using the QuadTree resampling technique (Lohman and Simons, 2005).

Figure 2. Data used for inversion and fits. (a) High-rate GNSS (HR-GNSS) waveforms. Black is observed, and red is modeled. Peak amplitude values are indicated next to each waveform. (b) Deepocean Assessment and Reporting of Tsunamis (DART) buoy pressure recording. Black is observed, red is modeled. (c) Downsampled Interferometric Synthetic Aperture Radar (InSAR) data for ascending track 107 and descending track 070 used for inversion. Shown are the observed, modeled, and residual fits. White star is the event hypocenter. LoS, Line of sight. The color version of this figure is available only in the electronic edition.

Tsunami data. We use tsunami observations from two tidegauge stations at Huatulco (HUAT, Fig. 1) and Salina Cruz (SALI, Fig. 3). The HUAT tide gauge samples at 6 min and recorded a significant co-seismic offset (Fig. 3). We removed the tidal signals using the TPXO9-atlas tidal model with 1/30 degree resolution interpolated at the location of the station (Egbert and Erofeeva, 2002), after that we estimated an uplift of 55 cm simply by taking the mean of 1 hr of data before the event and 1 hr after the earthquake. The record shows a negative value consistent with the sea level retreating in response to the coseismic deformation. The record at SALI has a faster sample rate (1 min) and was also corrected for tides. It shows no measurable coseismic offset.

To resolve shallow slip, we also use data from one ocean-bottom pressure sensor from station 43413 from the Deep-ocean Assessment and Reporting of Tsunamis (DART) network (Fig. 1). The data are sampled at 15 s and are band-pass filtered between 2 hr and 5 min to remove tides and surface wave arrivals, which produce noticeable pressure signals. After filtering, the record shows a small (0.5 cm) tsunami (Fig. 2).

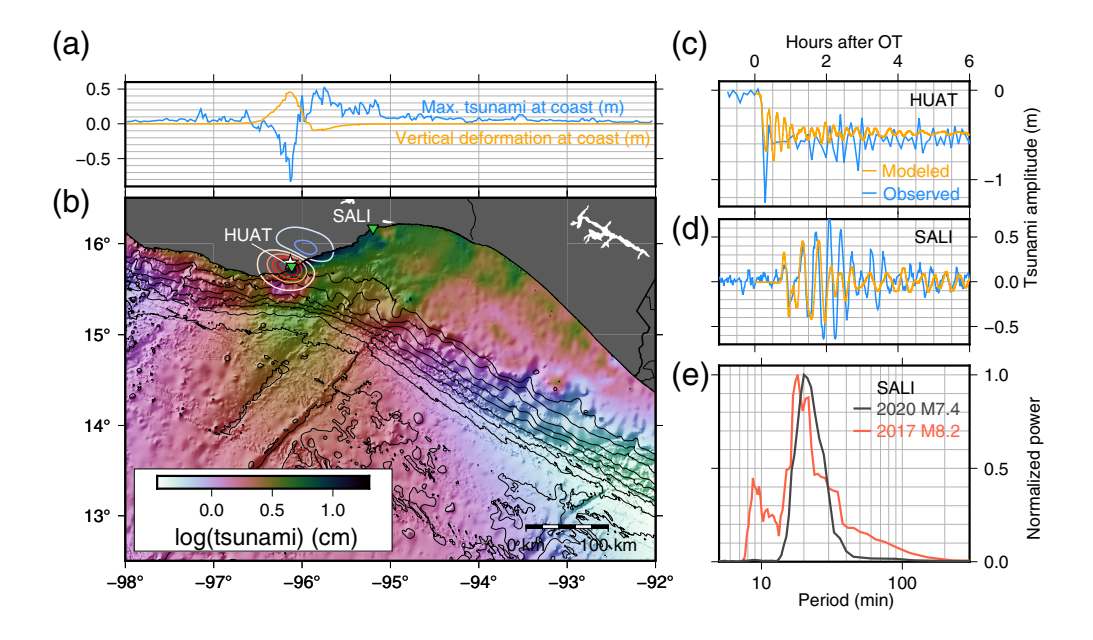


Figure 3. (a) Vertical coseismic deformation from the slip model at the coastline and maximum modeled tsunami amplitude at the coast. (b) Peak tsunami amplitude in the model domain. Contours are the coseismic vertical deformation from the slip model at 10 cm intervals, red is uplift, blue is subsidence. Locations of the HUAT and Salina Cruz (SALI) are shown. (c)–(d) Comparison between modeled and observed records at tide gauge locations. (e) Normalized amplitude spectrum at SALI, comparing the recorded tsunami in this event to that of the 2017 $M_{\rm w}$ 8.2 Tehuantepec earthquake. The color version of this figure is available only in the electronic edition.

Seismological data. We use two sets of regional data to study ground-motion intensities (Fig. 4). The first is from a network of MEMS accelerometers deployed by Grillo Sistemas, a private company using them for earthquake early warning. The sensors are triaxial, with an 18 bit digitizer, and are sampled at 32 Hz. We applied a basic baseline correction by removing the pre-event mean for each trace and high-pass filtering with a 20 s corner to remove baseline offsets. We also use strong-motion data from the regional network operated by the Instituto de Ingeniería at UNAM (II-UNAM). Raw data are not openly available, but processed intensities (peak ground acceleration [PGA] and spectral accelerations [SAs]) were obtained from the network's web page. For the energy and source spectrum estimation, we use the vertical component of 31 teleseismic stations at epicentral distances between 30° and 90°. We use a 60 s window around the P-wave group comprising the P, pP, and sP phases. We also study the aftershock distribution from the regional network catalog.

Modeling methods

Kinematic slip inversion. We perform a jointly kinematic inversion using the coseismic offset at the HUAT tide gauge, three-component displacement seismograms from 7 HR-GNSS stations along with the two InSAR scenes and one DART buoy waveform (Fig. 1). We use the linear multitime window approach implemented in the MudPy code and

described by Melgar and Bock (2015). We assume the Slab 2.0 geometry for the megathrust (Hayes et al., 2018) and discretize its 3D geometry into triangles of approximately 5 km sides using a finite element mesh. At the hypocentral region, the slab has an average strike of 278° and an average dip of 21°. We employ a radially symmetric Earth model used by Hernandez et al. (2001) for slip inversion of earthquakes in Southern Oaxaca. Green's functions for each data type are obtained using frequency-wave number integration for the deformation and waveform data and solving the shallow water equations for the tsunami data. The process is outlined in Melgar and Bock (2015). For rupture initiation, we use the local network hypocenter (-96.120°, 15.784°, 22.6 km), which is

closer to the coast than the hypocenter reported by the U.S. Geological Survey (USGS), which is about 16 km to the northeast of this location. This is a well-known bias of teleseismic hypocenters studied systematically by Hjörleifsdóttir et al. (2016) and observed for the 2017 $M_{\rm w}$ 8.2 Tehuantepec earthquake and its aftershocks as well (Melgar et al., 2018b). We run the inversion at several rupture speeds between (2.0 km/s and 4.0 km/s) and select the best fitting one. We use two sets of weights for the data, one to account for measurement uncertainties and one to account for the different sizes (quantified by the norms) of each data type. Details of this approach are in Text S1, which is available in the supplemental article. The rake is constrained to a window around pure thrust, and the inversion is solved using nonnegative least squares with Tikhonov (minimum-norm) regularization. The regularization parameter is chosen using the L-curve criterion.

Tsunami modeling. For tsunami modeling, we use the open source code GeoClaw (LeVeque *et al.*, 2011), which solves the nonlinear shallow water equations using a depth-averaged finite volume method. The initial condition is the vertical deformation from the slip model obtained using the triangular dislocation algorithm of Meade (2007). We assume that rupture is instantaneous, given that tsunami propagation is far slower than rupture velocity (Williamson *et al.*, 2019). Bathymetry and topography are a combination of SRTM15+

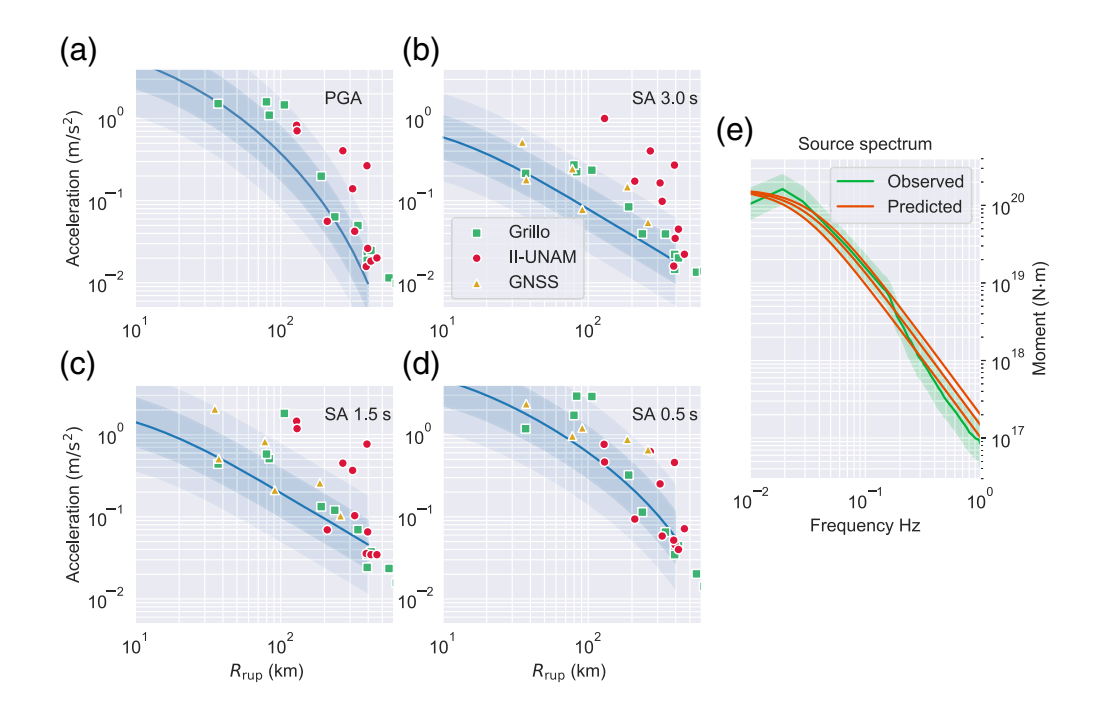


Figure 4. (a)–(d) Ground-motion intensities at Grillo micro-electromechanical (MEMS) accelerometer sites, HR-GNSS sites, and Instituto de Ingeniería at UNAM (II-UNAM) strong-motion sites. The reference line is the ground-motion model (GMM) of Arroyo *et al.* (2010) with one and two standard deviation regions shaded in. R_{rup} is the shortest distance to the slip model in Figure 1. (e) Observed far-field *P*-wave spectrum (green) with interquartile range shaded in as uncertainty. Red is the theoretical spectrum, based on the Brune (1970) model, assuming $M_0 = 1.60 \times 10^{20} \text{ N} \cdot \text{m}$, for a rupture with stress drop of 2.5, 3.0, and 3.5 MPa, respectively. The color version of this figure is available only in the electronic edition.

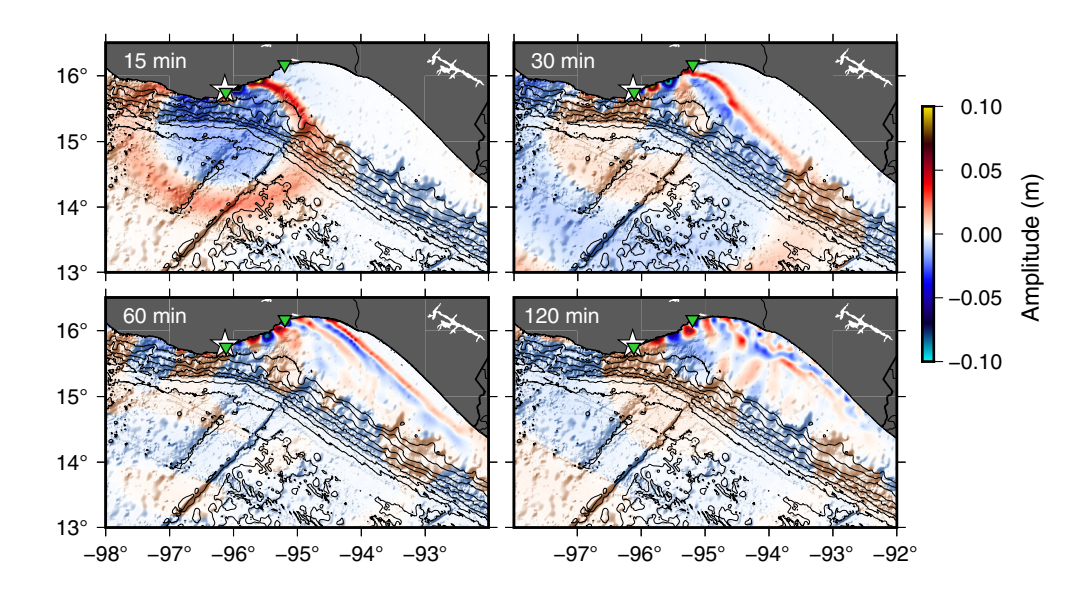


Figure 5. Snapshots of tsunami propagation from the model based on the coseismic deformation pattern of Figure 2a. The alternating lobes of positive and negative amplitude between HUAT and SALI (green triangles) are the edge wave modes. The white star is the event epicenter. The color version of this figure is available only in the electronic edition.

(Tozer et al., 2019), which has ~450 m onshore and offshore pixels with SRTM3, which has 90 m onshore-only pixels for more detailed shorelines. GeoClaw uses adaptive mesh refinement to dynamically refine the relevant regions of the model. We used six levels of refinement from an upper coarse level, with 10 arcmin resolution down to the final level with 3 arcsec resolution. At each step, the solver uses Courant-Friedrichs-Levy condition of 0.75, to ensure numerical stability. The tsunami model is run for 6 hr of model time using Manning's bottom-friction coefficient of 0.025. We collect model output at the locations of the two tide gauges as well as tracking the maximum amplitude of the tsunami at the coast and everywhere within the model domain (Figs. 3 and 5).

Far-field analysis, energy, and spectra. We follow Boatwright and Choy (1986), as modified by Pérez-Campos and Beroza (2001), to obtain the seismic energy from the teleseismic P-wave group records. The source spectrum was estimated by correcting the teleseismic data for the instrument response, attenuation, and site effect, assuming a very hard rock site, as defined by Boore and Joyner (1997) and suggested by Pérez-Campos et al. (2003). Figure 4e shows the source spectra and its confidence interval.

Ground-motion processing. Ground-motion intensities are obtained from the MEMS acceleration time series and from the HR-GNSS velocities. The MEMS are baseline

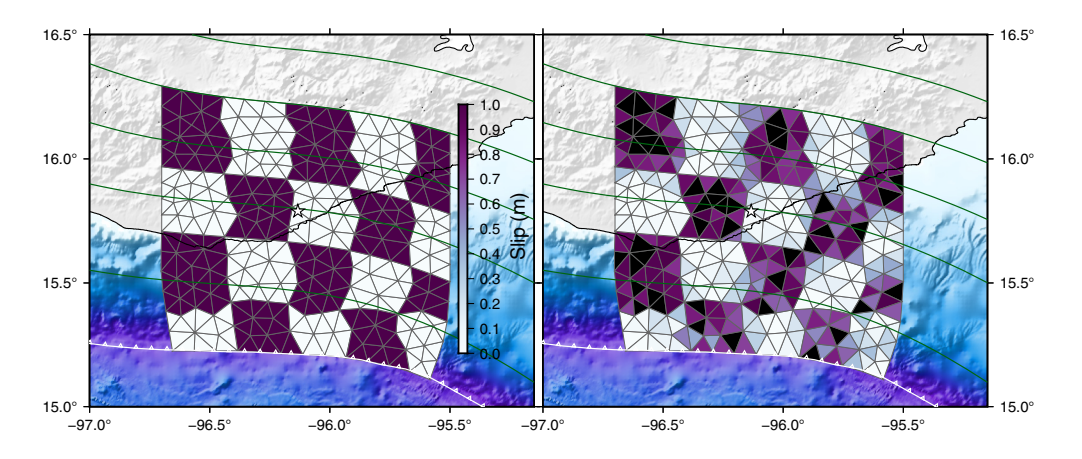


Figure 6. Inversion checkerboard test. Synthetic data using the input checkerboard (left) is generated using the same Green's functions used in the inversion. Realistic noise (estimated using the process in Text S2) is added to the synthetic data, and it is inverted using the preferred rupture speed and the same regularization parameter as that used in the final inversion. The results are shown in the right panel. White line is the trench and green liens are the slab contours at 10 km intervals. White star is the hypocenter. The color version of this figure is available only in the electronic edition.

corrected (see Seismological Data section) after which we extract the PGA as well as the SAs at several periods of interest (Fig. 4). The HR-GNSS velocities are differentiated to acceleration using a fourth-order finite difference scheme. Because the sample rate is 5 Hz, we do not extract SA for these data past the Nyquist frequency (2.5 Hz or 0.4 s). The SAs are obtained from the two horizontal components of motion using the RotD50 methodology, which takes the median value after rotating the accelerations through every possible orientation (Boore et al., 2006). We compare the observed intensities with those predicted by the ground-motion model (GMM) of Arroyo et al. (2010). As noted by Sahakian et al. (2018) during the 2017 earthquakes in Mexico, global GMMs underperform in Mexico compared with regional ones. The GMM of Arroyo et al. (2010) was designed specifically from megathrust events in Mexico, so it is a sensible choice.

Results

The slip distribution for the earthquake is compact with a single $\sim 60 \times 50$ km elliptical asperity with 5.3 m of peak slip. This is smaller than what is presented in the rapid USGS solution (~ 8 m). The final magnitude is $M_{\rm w}$ 7.37 (Fig. 1), which corresponds to a moment of 1.43×10^{20} N·m, which is slightly smaller than the Global Centroid Moment Tensor moment of 1.60×10^{20} N·m and larger than the USGS finite fault moment of 1.0×10^{20} N·m. The slip is well constrained in depth, with most of it occurring between 15 and 30 km. The source process lasts 15 s, with peak moment 5 s after rupture nucleation. The source time function shows multiple other peaks as well. This complexity occurs because even though the source is compact and confined to a single "asperity," the slip

within neighboring subfaults is still quite variable. The hypocenter is in the upper quarter of the rupture, so rupture propagates mostly down-dip of the initiation point and is bilateral along-strike. The preferred rupture speed is 3 km/s (Fig. S4), which corresponds to 75%-83% of shear-wave speed in the 1D Earth model. This is consistent with the mean of what is observed worldwide (e.g., Melgar and Hayes, 2017). The fits to the data are high with low-root mean square values to all data types (Fig. 2). Peak values for all the waveforms, both onshore and offshore, are well matched, and the residuals to the InSAR show no systematic biases.

Overall, this is a very well resolved slip model. Figure 6 shows the checkerboard test for resolution. The input checkers have 1 m of slip, and synthetic data were generated at the same sites using the same Green's functions as used in the inversion. The synthetic data is then contaminated with noise estimated by the process described in the previous section, and, inverted using the same hypocenter, data weights, rupture speed, and smoothing, as in the final inversion. The results show a very well resolved model. The checkers to the west are slightly better resolved than those to the east, which is not surprising, given that all but one of the HR-GNSS sites are to the west. Similarly, the checkers offshore show slightly lower resolution. However, thanks to the DART buoy data, the checkers are still recovered well without substantial over-smoothing (Fig. 6). One caveat is the fit to the HUAT tsunami signal. The static offset and the timing of the peaks are very well matched; this includes a large negative pulse. However, the amplitude of this pulse, we cannot model correctly. This potentially occurs due to the limited resolution near-shore bathymetry (as noted previously in Melgar and Ruiz-Angulo, 2018); or, perhaps, it is due to dynamic effects introduced into the tide-gauge mechanism by the intense shaking. We cannot say, for sure, at this stage.

Almost 90% of moment is released in the onshore portion of the fault, which explains the coseismic deformation pattern imaged by the InSAR. The fact that both the ascending and descending look directions show positive Line of Sight change is indicative of a large vertical component to the crustal deformation (Fig. 1). Indeed, the coseismic deformation model from the slip distribution (Fig. 2) shows uplift in the epicentral coastline with a peak value of 0.6 m. Subsidence occurs further inland and in the northeaster portion of the coast, with a peak

value of 0.15–0.2 m. This is also consistent with the 0.55 m of uplift measured at the HUAT tide gauge; the slip model predicts this well with a value of 0.52 m of uplift at this location.

The tsunami model shows an interesting pattern. Figure 3b shows the uplift and subsidence at the coastline, compared with the modeled peak tsunami amplitude. The coastline between -96.5° and -96° has a negative maximum peak tsunami amplitude, which correlates with the predominantly positive vertical coseismic deformation. This is confirmed by the tide-gauge recording from HUAT (Fig. 3c), which shows that although there are tsunami waves after the initial uplift signal, these are not large enough to overcome the initial vertical deformation; and, thus, the peak tsunami value remains negative. The tsunami model also shows that the amplitudes inside the Tehuantepec shelf (east of -96°) are systematically larger than outside of the shelf to the west of the source region. At the SALI tide-gauge recording, there are multiple large tsunami arrivals, with the peak value being reached until the fourth wave crest more than 2 hr after event origin time and ~80 min after the first tsunami arrival. This feature is captured well by the tsunami model, although the peak value is underestimated, and the energy decay is faster in the model than in the recorded signal. Snapshots of the model (Fig. 5) show that these repeated arrivals are from edge waves trapped near the coast between HUAT and SALI.

The ground-motion intensities (Fig. 4) are consistently higher than what is expected for an event of this magnitude. There are no values below the one-sigma uncertainty region, whereas there are many above the two-sigma uncertainty. The intensities from the strong-motion network (II-UNAM), which are mostly deployed within city basins, are much higher than for the MEMS or GNSS data. The far-field source spectrum (Fig. 4e) is nonetheless consistent with a stress drop between 2.5 and 3.5 MPa, which is close to the mean value when compared with other subduction events worldwide. Meanwhile the broadband energy magnitude is M_e 7.5, corresponding to $4.16 \times 10^{15} \pm 1.84 \times 10^{14}$ J, higher than what is expected for an $M_{\rm w}$ 7.4 earthquake and similar to that obtained by Incorporated Research Institutions for Seismology Data Management Center (IRIS DMC) (2013) EQEnergy $(4.1 \times 10^{15} \text{ J})$. As a result, the energy-to-moment ratio for this event is 2.53×10^{-5} , which is meaningfully higher than the global average of $\sim 1 \times 10^{-5}$ (Ye et al., 2016). This value is, however, only 1.3 times higher than for thrust events along the MSZ, as reported by Ordaz and Singh (1992), after considering a site effect factor (Plata-Martínez et al., 2019). The value is still 1.2 times higher than the ratio observed for the 2012 Ometepec-Pinotepa Nacional and 2018 Pinotepa earthquakes and their aftershocks closer to the coast (Plata-Martínez et al., 2019).

Discussion

The 2020 $M_{\rm w}$ 7.4 La Crucecita earthquake occurs in a region of the MSZ that is complex and exhibits both coseismic rupture

and SSEs. There is a limited overlap between the rupture area and the slow slip region identified in previous work (Fig. 1). Indeed, when this event is compared with other slip models and aftershocks areas, it is possible to conclude that rupture does not seem to penetrate past the 30 km depth contour. We posit this represents the down-dip edge of megathrust slip that generates significant seismic radiation for this part of the MSZ. Seismically detectable tectonic tremor occurs below this depth, but the low-frequency earthquakes that comprise tremor appear to be limited in fault dimension to magnitudes below M_w 3 (Brudzinski et al., 2010; Bostock et al., 2015). A comparison with the slip contours from the SSE preceding the 2012 M_w 7.5 Ometepec earthquake (Graham et al., 2014a, Fig. 1a) shows some potential overlap between the two. Extensive afterslip from the 2012 earthquake also indicates aseismic slip occurred within areas of previous coseismic rupture (Graham et al., 2014b). Dynamic models and recent observations show that under certain circumstances seismogenic rupture can penetrate areas previously dominated by slow slip (Ramos and Huang, 2019; Lin et al., 2020). In the MSZ, the resolution of the SSE models is modest, and geodetic coupling in this deep portion of the megathrust is low (Rousset et al., 2016), suggesting wholesale coseismic slip into the SSE region is limited and not a common occurrence. Neither this event nor the historical aftershock areas suggest it.

The event has features that are consistent with a rupture near the down-dip edge of slip. The rupture process has a stress drop that is comparable to other subduction zone events but an energy to moment ratio that places it in the upper limits of what is commonly seen in other similar events worldwide (Ye et al., 2016) and higher than the 2012 and 2018 events (Plata-Martínez et al., 2019). This is indicative of an efficient rupture process and can justify the systematically elevated ground motions. Similarly, the distribution of aftershocks for the first month after the event (Fig. 7) shows few events down-dip of where the mainshock slip terminates.

And yet the event was modestly tsunamigenic. This is not due to any shallow slip; the time-dependent waveform data and the DART buoy information are both sensitive to any shallow slip and produce a very well resolved slip model (Fig. 6), which conclusively discards this. The aftershocks confirm this as well (Fig. 7). Where the slip is high, the aftershock productivity is very low, as would be expected from the relaxation of the stress field. There is a region of large aftershock productivity immediately up-dip of the event, which stops short of the trench. Importantly, there is no significant outer rise seismicity, as would be expected from coulomb stress transfer had shallow slip on the megathrust occurred (Lay et al., 2011). This is even more striking given that for this portion of the middle America trench abyssal hill fabric that can be reactivated for seismogenic faulting is particularly prominent (e.g., Melgar et al., 2018b). Rather, the tsunamigenesis occurs because, whereas the MSZ has a very short continental shelf, the seismogenic

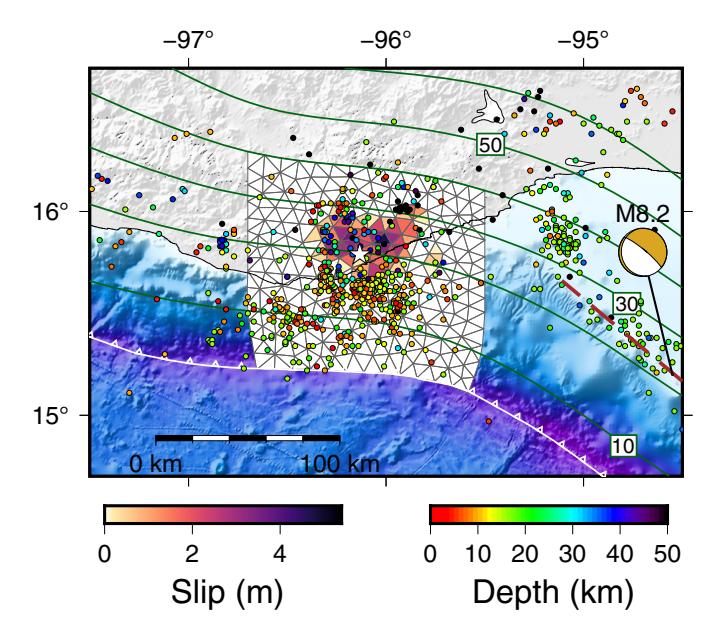


Figure 7. Distribution of aftershocks (circles) for the first month following the mainshock. White star is the mainshock hypocenter. The focal mechanism is for the 2017 $M_{\rm w}$ 8.2 Tehuantepec normal faulting event. The dashed line is the surface projection for that event's source fault (Melgar *et al.*, 2018a). Solid lines are the slab contours spaced every 10 km. The color version of this figure is available only in the electronic edition.

width is modest such that this "deep" event still produces some offshore deformation (Fig. 3a). In addition, at the source region, the coast juts to the north, widening the shelf and allowing for more of the coseismic deformation to occur offshore.

This peculiar configuration leads to a substantial portion of the coastline being uplifted and thus producing negative maximum peak tsunami amplitudes. During uplift, sea level drops and any resulting tsunami waves do not reach a high-enough amplitude to overcome this, as confirmed by the HUAT tide gauge (Fig. 3c). This is important, it is a clear example of why tsunamis are not always well recorded in the geologic record in Mexico. Specifically, in Oaxaca, none of the modern events dating back to at least 1965 (Fig. 1) seem to have any slip shallower than 10-15 km. This makes correctly assessing the tsunami hazard difficult. Is shallow slip possible? Suárez and Albini (2009) postulated from an analysis of historical data that the 1787 San Sixto earthquake, which occurred offshore Oaxaca, had a magnitude of ~M 8.6. Recently Ramírez-Herrera et al. (2020) identified tsunami deposits from this event several kilometers inland. Given the modest seismogenic width and the propensity of the coast in this part of the MSZ to uplift during rupture, it seems likely that to produce such long inundation distances, the 1787 event must have had substantial shallow slip. Singh et al. (1981, 1983) hypothesized that the Oaxaca segment of the MSZ fails repeatedly at semi-regular \sim 30–50 yr intervals on distinct asperities. Recent well-modeled events suggest there is some credence to this model, modern slip inversions regularly show overlap with aftershock areas of older events. In fact, the 2020 La Crucecita earthquake overlaps with a significant portion of the 1965 M 7.5 earthquake (UNAM seismology Group, 2013). However, if events of the size of the 1787 San Sixto earthquake are also possible, it suggests that any given earthquake does not release the entirety of the accumulated slip deficit. Instead, over many earthquake cycles, enough slip deficit can accumulate that neighboring asperities can fail together in one large event. The frequency with which this synchronization might occur is completely unknown. There is the added complexity that SSEs can potentially accelerate failure of an asperity (Graham et al., 2014a) so whether "super cycles" (Sieh et al., 2008) exist in the MSZ remains speculative. Finally, we note that the observations and modeling of the tsunami in the Gulf of Tehuantepec once more point to a higher hazard in this region compared with other parts of the MSZ. Melgar and Ruiz-Angulo (2018) noted that the morphology of the shelf is particularly prone to amplification by resonance and by trapping edge waves close to shore. The observed and modeled tide-gauge at SALI (Fig. 3) and snapshots of the tsunami model (Fig. 5) show a very welldeveloped edge wave train between HUAT and SALI during the 2020 event. A comparison of the spectra between the 2017 $M_{\rm w}$ 8.2 record and the 2020 record (Fig. 3e) shows that this same ~20 min spectral peak was excited in both events. Geodetic coupling in this part of the subduction zone has also been estimated to be high (Franco et al., 2012), and, if the seismogenic width is like other parts of the subduction zone then, because the shelf is far wider, we can expect wholesale subsidence of the coast during a future large event. This, compounded with the ability of the shelf to amplify and protract the duration of tsunamis, highlights the elevated hazard facing the Gulf of Tehuantepec region.

Conclusions

We find that the $M_{\rm w}$ 7.4 La Crucecita earthquake is completely contained between the 15 and 30 km depth contours. The rupture process is energetic, when compared with regional and global megathrust events. Based on this we posit that 30 km is likely the down-dip edge of coseismic rupture for this portion of the Mexican subduction interface. Up-dip of the hypocenter we conclusively rule out any shallow slip. The slip inversion includes multiple geophysical data sets and is very well constrained, even offshore. We find that it is the narrow seismogenic width and the peculiar configuration of the coastline that allow for a significant fraction of the coseismic deformation to occur offshore. The deep asperity is solely responsible for tsunamigenesis. The earthquake leads to significant uplift at the coast above it, which leads to negative maximum tsunami amplitudes and exemplifies why tsunamis are not always well recorded int eh geologic record in Mexico.

Finally, analysis of the tide-gauge recordings and tsunami propagation model shows how edge wave modes in the Gulf of Tehuantepec were excited and produce larger amplitudes and longer durations than elsewhere in the subduction zone.

Data and Resources

All the data and modeling codes in this article are openly available. GPS-Met data from the TLALOCNet archive are open and freely available at http://tlalocnet.udg.mx/tlalocnetgsac/. Access to the Sentinel-1 data is available through the European Space Agency (ESA) porta (https:// sentinel.esa.int/web/sentinel/sentinel-data-access). Grillo micro-electromechanical (MEMS) accelerometer data are available through Amazon Web Services at https://registry.opendata.aws/grillo-openeew/. Tide gauge data were provided by the Servicio Mareográfico Nacional of México (http://www.mareografico.unam.mx/portal/index.php?page= Estaciones). Servicio Sismológico Nacional (SSN) data products are from the Servicio Sismológico Nacional (México) and can be obtained at http://www2.ssn.unam.mx:8080/catalogo/. Strong-motion intensities were provided by the strong ground-motion database system and are the product of the Seismic Instrumentation group at the Instituto de Ingeniería of the Universidad Nacional Autónoma de México (II-UNAM) (https://aplicaciones.iingen.unam.mx/AcelerogramasRSM/ Registro.aspx). DART buoy data are provided by the National Oceanographic and Atmospheric Administration (https://www.ndbc .noaa.gov/dart.shtml). The processed high-rate Global Navigation Satellite System (HR-GNSS) and strong-motion waveforms, and the final slip model, are available in datasets in the supplemental material to this article. The slip inversion code MudPy, can be obtained from https:// github.com/dmelgarm/mudpy. The tsunami modeling code can be obtained from http://www.clawpack.org/. Teleseismic data, corresponding to II (Albuquerque Seismological Laboratory [ASL]/U.S. Geological Survey [USGS], 1980; Scripps Institution of Oceanography, 1986), IU (ASL/USGS, 1988), and G (Institut De Physique Du Globe De Paris [IPGP] and Ecole Et Observatoire Des Sciences De La Terre De Strasbourg [EOST], 1982) networks were downloaded from the Incorporated Research Institutions for Seismology Data Management Center (IRIS DMC). All websites were last accessed in July 2020.

Acknowledgments

This work was partially funded by National Aeronautics and Space Administration (NASA) Grant 80NSSC19K1104. The material is partly based on Global Positioning System or Global Navigation Satellite System (GPS/GNSS) data provided by the Trans-boundary Land and Atmosphere Long-term Observational and Collaborative Network (TLALOCNet) operated by Servicio de Geodesia Satelital from Instituto de Geofísica-UNAM in collaboration with UNAVCO Inc. and supported by National Science Foundation (NSF) Grant EAR-1724794; CONACyT Projects 253760 and 2017-01-5955; and UNAM-PAPIIT Projects IN104213, IN109315-3, and IN104818-3. Luis Salazar-Tlaczani at Servicio de Geodesia Satelital-UNAM provided invaluable support for the TLALOCNet field operations and stations maintenance. The authors thank the European Space Agency for access to the Sentinel-1 data. SSN data products station maintenance, data acquisition, and distribution are thanks to its personnel. The authors also thank Sebastian Riquelme for discussions on the slip model and for sharing his early findings.

References

- Albuquerque Seismological Laboratory (ASL)/U.S. Geological Survey (USGS) (1980). US Geological Survey Networks, International Federation of Digital Seismograph Networks, doi: 10.7914/SN/GS.
- Albuquerque Seismological Laboratory (ASL)/U.S. Geological Survey (USGS) (1988). Global Seismograph Network (GSN IRIS/USGS), International Federation of Digital Seismograph Networks, Other/ Seismic Network, doi: 10.7914/SN/IU.
- Arroyo, D., D. García, M. Ordaz, M. A. Mora, and S. K. Singh (2010). Strong ground-motion relations for Mexican interplate earth-quakes, *J. Seismol.* **14**, no. 4, 769–785.
- Astiz, L., and H. Kanamori (1984). An earthquake doublet in Ometepec, Guerrero, Mexico, *Phys. Earth Planet. In.* **34**, nos. 1/2, 24–45.
- Boatwright, J., and G. Choy (1986). Teleseismic estimates of the energy radiated by shallow earthquakes, *J. Geophys. Res.* **91**, 2095–2112.
- Boore, D. M., and W. B. Joyner (1997). Site amplifications for generic rock sites, *Bull. Seismol. Soc. Am.* **87,** 327–341.
- Boore, D. M., J. Watson-Lamprey, and N. A. Abrahamson (2006). Orientation-independent measures of ground motion, *Bull. seismol. Soc. Am.* 96, no. 4A, 1502–1511.
- Bostock, M. G., A. M. Thomas, G. Savard, L. Chuang, and A. M. Rubin (2015). Magnitudes and moment-duration scaling of low-frequency earthquakes beneath southern Vancouver Island, *J. Geophys. Res.* **120**, no. 9, 6329–6350.
- Brudzinski, M. R., H. R. Hinojosa-Prieto, K. M. Schlanser, E. Cabral-Cano, A. Arciniega-Ceballos, O. Diaz-Molina, and C. DeMets (2010). Nonvolcanic tremor along the Oaxaca segment of the Middle America subduction zone, J. Geophys. Res. 115, B00A23.
- Brune, J. N. (1970). Tectonic stress and the spectra of seismic shear waves from earthquakes, *J. Geophys. Res.* **75**, no. 26, 4997–5009.
- Cabral-Cano, E., X. Pérez-Campos, B. Márquez-Azúa, M. A. Sergeeva,
 L. Salazar-Tlaczani, C. DeMets, D. Adams, J. Galetzka, K. Hodgkinson, K. Feaux *et al.* (2018). TLALOCNet: A continuous GPS-Met backbone in Mexico for seismotectonic and atmospheric research, *Seismol. Res. Lett.* 89, no. 2A, 373–381.
- Chael, E. P., and G. S. Stewart (1982). Recent large earthquakes along the middle American trench and their implications for the subduction process, *J. Geophys. Res.* **87**, 329–338.
- Chen, C. W., and H. A. Zebker (2002). Phase unwrapping for large SAR interferograms: Statistical segmentation and generalized network models, *IEEE Trans. Geosci. Rem. Sens.* 40, no. 8, 1709–1719, doi: 10.1109/TGRS.2002.802453.
- Colella, H. V., S. M. Sit, S. M. Brudzinski, S. E. Graham, C. DeMets, S. G. Holtkamp, R. J. Skoumal, N. Ghouse, E. Cabral-Cano, V. Kostoglodov, et al. (2017). Seismicity rate increases associated with slow slip episodes prior to the 2012 M_w 7.4 Ometepec earthquake, Earth Planet. Sci. Lett. 464, 35–45, doi: 10.1016/j.epsl.2016.12.032.
- Colosimo, G., M. Crespi, and A. Mazzoni (2011). Real-time GPS seismology with a stand-alone receiver: A preliminary feasibility demonstration, *J. Geophys. Res.* 116, no. B11, doi: 10.1029/ 2010JB007941.
- Corona, N., and M. T. Ramírez-Herrera (2012). Mapping and historical reconstruction of the great Mexican 22 June 1932 tsunami, *Nat. Hazards Earth Syst. Sci.* **12**, no. 5, 1337.
- Courboulex, F., M. A. Santoyo, J. F. Pacheco, and S. K. Singh (1997). The 14 September 1995 (M = 7.3) Copala, Mexico, earthquake:

- A source study using teleseismic, regional, and local data, *Bull. Seismol. Soc. Am.* **87**, no. 4, 999–1010.
- DeMets, C., R. G. Gordon, and D. F. Argus (2010). Geologically current plate motions, *Geophys. J. Int.* **181**, no. 1, 1–80.
- Egbert, G. D., and S. Y. Erofeeva (2002). Efficient inverse modeling of barotropic ocean tides, *J. Atmos. Ocean. Tech.* **19**, no. 2, 183–204.
- Franco, A., C. Lasserre, H. Lyon-Caen, V. Kostoglodov, E. Molina, M. Guzman-Speziale, D. Monterosso, V. Robles, C. Figueroa, W. Amaya, et al. (2012). Fault kinematics in northern Central America and coupling along the subduction interface of the Cocos Plate, from GPS data in Chiapas (Mexico), Guatemala and El Salvador, Geophys. J. Int. 189, no. 3, 1223–1236.
- Graham, S. E., C. DeMets, E. Cabral-Cano, V. Kostoglodov, A. Walpersdorf, N. Cotte, M. Brudzinski, R. McCaffrey, and L. Salazar-Tlaczani (2014a). GPS constraints on the 2011–2012 Oaxaca slow slip event that preceded the 2012 March 20 Ometepec earthquake, southern Mexico, Geophys. J. Int. 197, no. 3, 1593–1607.
- Graham, S. E., C. DeMets, E. Cabral-Cano, V. Kostoglodov, A. Walpersdorf, N. Cotte, M. Brudzinski, R. McCaffrey, and L. Salazar-Tlaczani (2014b). GPS constraints on the Mw=7.5 Ometepec earthquake sequence, southern Mexico: Coseismic and postseismic deformation, *Geophys. J. Int.* 199, no. 1, 200–218.
- Graham, S., C. DeMets, E. Cabral-Cano, V. Kostoglodov, B. Rousset, A. Walpersdorf, N. Cotte, C. Lasserre, R. McCaffrey, and L. Salazar-Tlaczani (2015). Slow slip history for the Mexico subduction zone: 2005 through 2011, in Geodynamics of the Latin American Pacific Margin, Birkhäuser, Cham, 3445–3465.
- Hayes, G. P., G. L. Moore, D. E. Portner, M. Hearne, H. Flamme, M. Furtney, and G. M. Smoczyk (2018). Slab2, a comprehensive subduction zone geometry model, *Science* 362, no. 6410, 58–61.
- Hernandez, B., N. M. Shapiro, S. K. Singh, J. F. Pacheco, F. Cotton, M. Campillo, A. Iglesias, V. Cruz, J. M. Gómez, and L. Alcántara (2001). Rupture history of September 30, 1999 intraplate earth-quake of Oaxaca, Mexico (Mw= 7.5) from inversion of strong-motion data, *Geophys. Res. Lett.* 28, no. 2, 363–366.
- Herring, T. A., R. W. King, and S. C. McClusky (2010). *Introduction to Gamit/Globk*. Massachusetts Institute of Technology, Cambridge, Massachusetts.
- Hjörleifsdóttir, V., S. K. Singh, and A. Husker (2016). Differences in epicentral location of Mexican earthquakes between local and global catalogs: An update, *Geofis. Int.* 55, no. 1, 79–93.
- Institut De Physique Du Globe De Paris (IPGP) and Ecole Et Observatoire Des Sciences De La Terre De Strasbourg (EOST) (1982). GEOSCOPE, French Global Network of Broad Band Seismic Stations, Institut de Physique du Globe de Paris (IPGP), doi: 10.18715/geoscope.g.
- Incorporated Research Institutions for Seismology Data Management Center (IRIS DMC) (2013). Data Services Products: EQEnergy Earthquake energy & rupture duration, doi: 10.17611/DP/EQE.1.
- Kostoglodov, V., S. K. Singh, J. A. Santiago, S. I. Franco, K. M. Larson, A. R. Lowry, and R. Bilham (2003). A large silent earthquake in the Guerrero seismic gap, Mexico, *Geophys. Res. Lett.* **30**, no. 15.
- Lay, T., C. J. Ammon, H. Kanamori, M. J. Kim, and L. Xue (2011). Outer trench-slope faulting and the 2011 M w 9.0 off the Pacific coast of Tohoku Earthquake, Earth Planet. Space 63, no. 7, 37.

- LeVeque, R. J., D. L. George, and M. J. Berger (2011). Tsunami modelling with adaptively refined finite volume methods, *Acta Numerica* **20**, 211.
- Li, Y., X. Shan, C. Zhu, X. Qiao, L. Zhao, and C. Qu (2020). Geodetic Model of the 2018 M w 7.2 Pinotepa, Mexico, Earthquake Inferred from InSAR and GPS Data, *Bull. Seismol. Soc. Am.* 110, no. 3, 1115–1124.
- Lin, J. T., K. S. Aslam, A. M. Thomas, and D. Melgar (2020). Overlapping regions of coseismic and transient slow slip on the Hawaiian décollement, *Earth Planet. Sci. Lett.* 544, 116,353.
- Lohman, R. B., and M. Simons (2005). Some thoughts on the use of InSAR data to constrain models of surface deformation: Noise structure and data downsampling, *Geochem. Geophys. Geosyst.* 6, no. 1, doi: 10.1029/2004GC000841.
- Meade, B. J. (2007). Algorithms for the calculation of exact displacements, strains, and stresses for triangular dislocation elements in a uniform elastic half space, *Comput. Geosci.* 33, no. 8, 1064–1075.
- Melgar, D., and Y. Bock (2015). Kinematic earthquake source inversion and tsunami runup prediction with regional geophysical data, *J. Geophys. Res.* **120**, no. 5, 3324–3349.
- Melgar, D., and G. P. Hayes (2017). Systematic observations of the slip pulse properties of large earthquake ruptures, *Geophys. Res. Lett.* **44**, no. 19, 9691–9698.
- Melgar, D., and X. Pérez-Campos (2011). Imaging the Moho and subducted oceanic crust at the Isthmus of Tehuantepec, Mexico, from receiver functions, *Pure Appl. Geophys.* **168**, nos. 8/9, 1449–1460.
- Melgar, D., and A. Ruiz-Angulo (2018). Long-lived tsunami edge waves and shelf resonance from the M8.2 Tehuantepec earthquake, *Geophys. Res. Lett.* **45**, no. 22, 412–414.
- Melgar, D., A. Ruiz-Angulo, E. S. Garcia, M. Manea, V. C. Manea, X. Xu, M. T. Ramirez-Herrera, J. Zavala-Hidalgo, J. Geng, N. Corona, et al. (2018a). Deep embrittlement and complete rupture of the lithosphere during the Mw 8.2 Tehuantepec earthquake, Nat. Geosci. 11, no. 12, 955–960.
- Melgar, D., X. Pérez-Campos, L. Ramirez-Guzman, Z. Spica, V. H. Espíndola, W. C. Hammond, and E. Cabral-Cano (2018b). Bend faulting at the edge of a flat slab: The 2017 Mw7. 1 Puebla-Morelos, Mexico earthquake, *Geophys. Res. Lett.* 45, no. 6, 2633–2641.
- Ordaz, M., and S. K. Singh (1992). Source spectra and spectral attenuation of seismic waves from Mexican earthquakes and evidence of amplification in the hill zone of Mexico City, *Bull. Seismol. Soc. Am.* **82**, 24–43.
- Pardo, M., and G. Suárez (1995). Shape of the subducted Rivera and Cocos plates in southern Mexico: Seismic and tectonic implications, *J. Geophys. Res.: Solid Earth* **100**, no. B7, 12,357–12,373.
- Pérez-Campos, X., and G. C. Beroza (2001). An apparent mechanism dependence of radiated seismic energy, *J. Geophys. Res.* **106**, 11,127–11,136.
- Pérez-Campos, X., S. K. Singh, and G. C. Beroza (2003). Reconciling teleseismic and regional estimates of seismic energy, *Bull. Seismol. Soc. Am.* **93**, 2123–2130.
- Plata-Martínez, R., X. Pérez-Campos, and S. K. Singh (2019). Spatial distribution of radiated seismic energy of three aftershocks sequences at Guerrero, Mexico, subduction zone, *Bull. Seismol. Soc. Am.* 109, no. 6, 2556–2566.

- Ramírez-Herrera, M., N. Corona, J. Cerny, R. Castillo-Aja, D. Melgar, M. Lagos, A. Goguitchaichvili, M. L. Machain, M. L. Vazquez-Caamal, M. Ortuño, et al. (2020). Sand deposits reveal great earthquakes and tsunamis at Mexican Pacific Coast, Sci. Rept. 10, 11,452, doi: 10.1038/s41598-020-68237-2.
- Ramírez-Herrera, M. T., N. Corona, A. Ruiz-Angulo, D. Melgar, and J. Zavala-Hidalgo (2018). The 8 September 2017 tsunami triggered by the M w 8.2 intraplate earthquake, Chiapas, Mexico, *Pure Appl. Geophys.* 175, no. 1, 25–34.
- Ramírez-Herrera, M. T., M. Lagos, I. Hutchinson, V. Kostoglodov, M. L. Machain, M. Caballero, A. Goguitchaichvili, B. Aguilar, C. Chague-Goff, J. Goff, et al. (2012). Extreme wave deposits on the Pacific coast of Mexico: Tsunamis or storms?—A multiproxy approach, Geomorphology 139, 360–371.
- Ramos, M. D., and Y. Huang (2019). How the transition region along the Cascadia megathrust influences coseismic behavior: Insights from 2-D dynamic rupture simulations, *Geophys. Res. Lett.* 46, no. 4, 1973–1983.
- Rousset, B., M. Campillo, C. Lasserre, W. B. Frank, N. Cotte, A. Walpersdorf, and V. Kostoglodov (2017). A geodetic matched filter search for slow slip with application to the Mexico subduction zone, *J. Geophys. Res.* 122, no. 12, 10–498.
- Rousset, B., C. Lasserre, N. Cubas, S. Graham, M. Radiguet, C. DeMets, and N. Cotte (2016). Lateral variations of interplate coupling along the Mexican subduction interface: Relationships with long-term morphology and fault zone mechanical properties, *Pure Appl. Geophys.* **173**, nos. 10/11, 3467–3486.
- Sahakian, V. J., D. Melgar, L. Quintanar, L. Ramírez-Guzmán, X. Pérez-Campos, and A. Baltay (2018). Ground motions from the 7 and 19 September 2017 Tehuantepec and Puebla-Morelos, Mexico, earthquakes, *Bull. Seismol. Soc. Am.* 108, no. 6, 3300–3312.
- Sandwell, D. T., X. Xu, R. Mellors, M. Wei, X. Tong, and P. Wessel (2016). GMTSAR: An InSAR processing system based on Generic Mapping Tools, Second Edition, University of California San Diego, La Jolla, California, available at http://topex.ucsd.edu/ gmtsar/tar/GMTSAR_2ND_TEX.pdf.
- Scripps Institution of Oceanography (1986). IRIS/IDA seismic network, International Federation of digital seismograph networks, other/seismic network, doi: 10.7914/SN/II.
- Sieh, K., D. H. Natawidjaja, A. J. Meltzner, C. C. Shen, H. Cheng, K. S. Li, B. W. Suwargadi, J. Galetzka, B. Philibosian, and R. L. Edwards (2008).

- Earthquake supercycles inferred from sea-level changes recorded in the corals of west Sumatra, *Science* **322**, no. 5908, 1674–1678.
- Singh, S. K., L. Astiz, and J. Havskov (1981). Seismic gaps and recurrence periods of large: A reexamination earthquakes along the Mexican subduction zone, *Bull. Seismol. Soc. Am.* 71, no. 1981, 827–843.
- Singh, S. K., M. Rodríguez, and L. Esteva (1983). Statistics of small earthquakes and frequency of occurrence of large earthquakes along the Mexican subduction zone, *Bull. Seismol. Soc. Am.* **73**, 1779–1796.
- Suárez, G., and P. Albini (2009). Evidence for great tsunamigenic earthquakes (M 8.6) along the Mexican subduction zone, *Bull. Seismol. Soc. Am.* 99, no. 2A, 892–896.
- Suárez, G., M. A. Santoyo, V. Hjörleifsdóttir, A. Iglesias, C. Villafuerte, and V. M. Cruz-Atienza (2019). Large scale lithospheric detachment of the downgoing Cocos plate: The 8 September 2017 earthquake (Mw 8.2), Earth and Planet. Sci. Lett. 509, 9–14.
- Tozer, B., D. T. Sandwell, W. H. F. Smith, C. Olson, J. R. Beale, and P. Wessel (2019). Global bathymetry and topography at 15 arc sec: SRTM15+, *Earth Space Sci.* **6**, no. 10, 1847–1864.
- UNAM Seismology Group (2013). Ometepec-Pinotepa Nacional, Mexico Earthquake of 20 March 2012 (Mw 7.5): A preliminary report, *Geofis. Int.* **52**, no. 2, 173–196.
- Williamson, A., D. Melgar, and D. Rim (2019). The Effect of earth-quake kinematics on Tsunami propagation, *J. Geophys. Res.* **124**, no. 11, 11,639–11,650.
- Wessel, P., J. F. Luis, L. Uieda, R. Scharroo, F. Wobbe, W. H. F. Smith, and D. Tian (2019). The generic mapping tools version 6, Geochem. Geophys. Geosyst. 20, no. 11, 5556–5564.
- Xu, X., D. T. Sandwell, E. Tymofyeyeva, A. González-Ortega, and X. Tong (2017). Tectonic and anthropogenic deformation at the Cerro Prieto geothermal step-over revealed by Sentinel-1A InSAR, *IEEE Trans. Geosci. Rem. Sens.* 55, no. 9, 5284–5292, doi: 10.1109/ TGRS.2017.2704593.
- Ye, L., T. Lay, H. Kanamori, and L. Rivera (2016). Rupture characteristics of major and great ($Mw \ge 7.0$) megathrust earthquakes from 1990 to 2015: 1. Source parameter scaling relationships, *J. Geophys. Res.* **121**, no. 2, 826–844.

Manuscript received 4 August 2020 Published online 14 October 2020